Shrinking-core modeling of binary chromatographic breakthrough

Steven J. Traylor, Xuankuo Xu [1], Abraham M. Lenhoff*

Department of Chemical Engineering, University of Delaware, Newark, DE 19716, USA

ARTICLE INFO

ABSTRACT

Most chromatographic processes involve separation of two or more species, so development of a simple, accurate multicomponent chromatographic model can be valuable for improving process efficiency and yield. We consider the case of breakthrough chromatography, which has been considered in great depth for single-component modeling but to a much more limited degree for multicomponent breakthrough. We use the shrinking core model, which provides a reasonable approximation of particle uptake for proteins under strong binding conditions. Analytical column solutions for single-component systems are extended here to predict binary breakthrough chromatographic behavior for conditions under which the external transport resistance is negligible. Analytical results for the location and profile of displacement effects and expected breakthrough curves are derived for limiting cases. More generally, straightforward numerical results have also been obtained through simultaneous solution of a set of simple ordinary differential equations. Exploration of the model parameter space yields results consistent with theoretical expectations. Additionally, both analytical and numerical predictions compare favorably with experimental column breakthrough data for lysozyme–cytochrome c mixtures on the strong cation exchanger SP Sepharose FF. Especially significant is the ability of the model to predict experimentally observed displacement profiles of the more weakly adsorbed species (in this case cytochrome c). The ability to model displacement behavior using simple analytical and numerical techniques is a significant improvement over current methods.

© 2011 Elsevier B.V. All rights reserved.

1. Introduction

Within the non-linear chromatography regime, much attention has been devoted to both analytical and numerical solution methods for modeling single-component processes, but significantly less success has been achieved in deriving efficient solution methods for models of multicomponent separations. In particular, for modeling chromatography of proteins and other strongly adsorbed molecular species, the general principles and phenomena involved in binary breakthrough and displacement are well known, but appropriate mechanistic descriptions are not always compatible with efficient solution methods. Here we describe such a solution method for column loading via an extension to binary systems of the well-known shrinking core model of uptake behavior.

For breakthrough experiments, in which the column is loaded to its equilibrium capacity with a single or multiple species, the key to an efficient solution for single-component analysis is often the constant-pattern limit, in which a shock profile that develops within a column eventually becomes invariant with time [1,2]. A number of analytical solutions and approximations have been developed, assuming a variety of combinations of isotherms and limiting mass transfer effects. Single-component analytical solutions have been derived for irreversible isotherms assuming behavior limited by adsorption kinetics [1] or solid (homogeneous) diffusion [3,4]. Additional analytical solutions have been derived assuming a Langmuir isotherm and solid [3,5] and liquid [3,6] linear driving force models. Analytical approximations and representative numerical solutions have also been obtained for both solid- and pore-diffusion cases assuming Langmuir isotherms [7]. Based on this work, Cooper and Liberman [8] developed a complete analytical column solution, not dependent on a constant-pattern assumption but assuming a rectangular isotherm and pore-diffusion controlled uptake behavior, resulting in shrinking-core particle saturation profiles similar to those illustrated in Fig. 1. Additional analytical solutions include the Thomas model, which assumes a second-order reaction kinetic model [9,10]. A more inclusive model would require numerical solution of the general rate model, which is computationally expensive [3].

Relatively few analytical solutions of multicomponent breakthrough chromatography have been reported. The topic was introduced by Glueckauf, who considered multicomponent equilibrium behavior [11]. The existence of multicomponent constant-pattern regions was proven by Cooney and Lightfoot [12], who went on to solve analytically the solid-film linear driving force case [13], and

---

* Corresponding author. Tel.: +1 302 831 8989.
  E-mail address: lenhoff@udel.edu (A.M. Lenhoff).
[1] Current address: Bristol-Myers Squibb, 6000 Thompson Road, East Syracuse, NY 13057, USA.
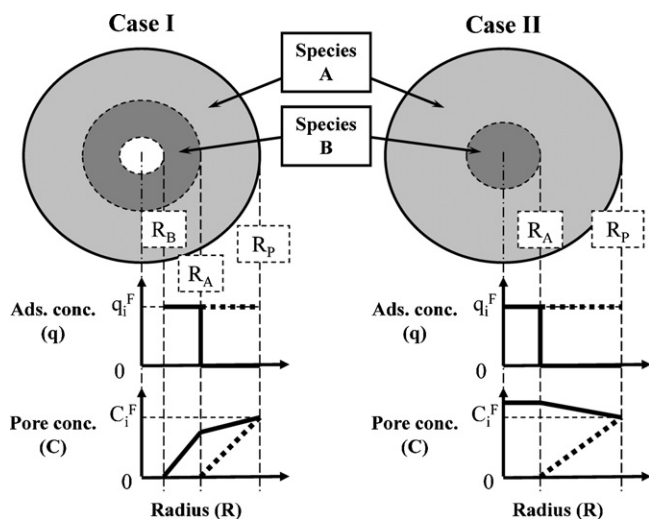
Fig. 1. Schematic of binary shrinking core uptake, adapted from [36]. The outer shell corresponds to species *A* and the inner to species *B*. The fluid and solid phase concentrations are represented by C_i and q_i, respectively. Concentration profiles of species *A* are denoted by dashes and those of species *B* by solid lines. The superscript *F* denotes the bulk mobile phase concentration and the adsorbed concentration in equilibrium with it.

later solved in more detail a similar system assuming a multicomponent Langmuir isotherm [14]. A key assumption in many of these models involves deriving an analytical expression relating concentrations of multiple components in displacement regions and using these relationships to simplify isotherms to pseudo-binary form [14]. Similar analytical treatments of this type have been derived for the solid-film [15] and both solid- and liquid-film [16,17] linear driving force models.

The most comprehensive analytical treatment of multicomponent chromatography is that of Rhee and Amundsen [18], which assumes a solid-film linear driving force and accounts for axial dispersion effects using a h-transform solution approach [19–21]. Shock wave thickness and propagation velocities are estimated in this model, as well as limiting concentrations of each species between the shock layers [3,18]. The limitations of this model include its mathematical complexity and its limitations on and lumping of intraparticle transport effects. A similar approach has been applied to estimating shock layer thickness based on the equilibrium-dispersive model and has been extended to investigate the formation of displacement layer (concentration overshoot) effects [22]. A number of efforts to model breakthrough and displacement have resorted to numerical solutions of the general rate model assuming pore diffusion and a multicomponent isotherm [23–27], among others. A comprehensive summary of both analytical and numerical work in this area is available [28].

A weakness inherent to many of the existing multicomponent constant-pattern solutions is the lack of clearly defined existence conditions for constant-pattern behavior, i.e., the column length necessary to attain the constant pattern. This topic has been considered in some detail using analytical approximations within the framework of the linear driving force model [13,17] as well as numerically and experimentally [29,30]. Without such guidance, the constant-pattern assumption may be limited in its applicability for predicting column behavior.

A useful limiting model can be developed from the assumption of irreversible adsorption, which results in a rectangular isotherm that, when applied to pore diffusion-limited uptake, results in the shrinking-core model [7,8]. These assumptions have been validated by confocal microscopy and other techniques for studying the single-component uptake of proteins on ion-exchange resins

under strongly binding conditions [31–35]. For multicomponent systems under strongly binding conditions the isotherms may still be near-rectangular, but competitive adsorption often appears to indicate almost complete displacement of a less strongly bound component by a more strongly bound one [36,37]. These results suggest that under the observed conditions, assuming rectangular isotherms may be appropriate for describing multicomponent column behavior. The adsorbed concentration of a more weakly bound component will then depend partly on whether any of a more strongly bound component is present to displace it completely or partially from the adsorbent. Here we use this approach for binary systems, with component *A* more strongly bound than component *B*; in some of the literature the alternative convention is used in which species *A* is expected to bind more weakly than and elute before species *B* [14,21,38].

Assumption of rectangular isotherms in a binary batch uptake system allows application of the binary shrinking-core model, which follows the standard theory [39–41] but includes modification to account for displacement of *B* at the adsorption front for *A* [36]. Fig. 1 illustrates uptake within a particle, with the outer shell representing the displacing species *A* and the inner shell the displaced species *B*. After the particle is saturated with *B*, displacement continues to occur, and results in concentration overshoot effects within the particle, represented in the lower right graph.

In order to develop a binary breakthrough model that is both efficient and capable of accounting for strong binding and displacement effects, we have extended the multicomponent batch shrinking core model [36] to the column framework for which a general single-component breakthrough solution was developed by Cooper and Liberman [8]. The resulting approach requires numerical integration in certain cases, but the structure provided by the single-component solution makes this method more efficient than a fully numerical solution, for which the sharp fronts and consequent steep gradients present important difficulties.

2. Materials and methods

2.1. Materials

All chemicals and proteins were obtained from Sigma (St. Louis, MO) and used without further purification. Phosphate-buffered saline (PBS) was prepared using 10 mM sodium phosphate (19.9 mM ionic strength, I.S.) and adjusted to pH 7 using 1 M hydrochloric acid or sodium hydroxide. All buffers were prepared at room temperature (23 ± 2 °C) using deionized water from a Millipore Milli-Q system (>18.2 MΩ cm) and filtered with 0.22 μm Gelman VacuCap bottle-top filters (Pall Corporation, Ann Arbor, MI).

Chicken egg white lysozyme (LYS) (L6875, lot 093k1455 and L6876, lot 051K7028) and cytochrome c (CYC) from bovine heart (C3131, lot 083k7037 and C2037, lot 61K7018) were obtained from Sigma with manufacturer-reported purities of 95% and 97%, respectively. Protein solutions were prepared in the 0 mM NaCl PBS buffer, filtered with 0.22 μm Millipore Millex-GV filters (Millipore Corporation, Bedford, MA), and stored at 4 °C. All protein solutions were further filtered before use to remove possible aggregates formed during preparation or storage. Protein concentrations were determined via spectrophotometry, with the relative amounts of both proteins determined by using simultaneous absorbance measurements at 280 nm and 405 nm.

The cation-exchange resin used was SP Sepharose FF (lots 297051 and 10020387), an agarose-based material (GE Healthcare, Piscataway, NJ). Protein and resin behavior was compared between lots to verify similarity.

2.2. Apparatus

A 0.35 mL Omnifit microbore glass chromatography column (P.J. Cobert Associates, Inc., St. Louis, MO), 0.3 cm i.d. × 5.0 cm long, and a 1.19 mL AP Minicolumn glass chromatography column (Waters Corporation, Milford, MA), 0.5 cm i.d. × 6.1 cm long, packed with SP Sepharose FF particles was used to obtain frontal loading profiles on an ÄKTA Explorer 100 (GE Healthcare). A sample pump P-960 was used to feed the protein solution.

2.3. Methods

Adsorbent particles were washed three times with a 1.0 M NaOH solution or a 1.0 M NaCl solution. Helium was used to degas the slurry prior to column packing with a high-salt buffer. The slurry was gravity-packed in 1.0 M NaCl and subsequently flow packed for 15 min at a superficial velocity of 610 cm/h in 1.0 M NaCl.

The UV response of the feed protein concentrations was determined by bypassing the column and monitoring the detector response. The column was then equilibrated with 10 column volumes of 0 mM NaCl PBS buffer, and the protein solution was loaded directly onto the column using the sample pump while the output was monitored. After each run was terminated, the column was washed with 10 column volumes of 1.0 M NaCl buffer.

3. Theory

The single-component shrinking core column solution [4,7,8] was derived in terms of two dimensionless independent variables, a dimensionless time Θ and a dimensionless column position N, defined as

$$\Theta = \frac{6D_e^A(1-\varepsilon)}{\Lambda_A R_p^2}\left(t - \frac{z}{u}\right) \tag{1}$$

$$N = \frac{6D_e^A}{R_p^2}\frac{1-\varepsilon}{\varepsilon}\frac{z}{u} \tag{2}$$

The dimensionless variables and parameters are based on those introduced by Vermeulen [4] and by Hall et al. [7], but they have been modified to maintain consistency with the notation of Martin et al. [36], which simplifies the results. At the column entrance, the dimensionless time Θ simplifies to that used by Martin et al. For the sake of brevity, key results from the derivation are presented here and additional details are made available as Supplementary Information.

It is useful to consider the qualitative form of the solution within the (N, Θ) domain (Fig. 2). The binary shrinking-core solution for a single particle [36] represents the column entrance behavior ($N = 0$) on the left-hand ordinate of Fig. 2. Uptake occurs between the lines indicated, with the unlabeled zones representing saturation (upper left and center) or depletion regions (lower right). Initially, both species A and B are adsorbed on the column at the same time, but as time passes, species B is both fed and displaced, and enough excess B accumulates to travel ahead of the species A front and create a saturated region of adsorbed B, which is subsequently displaced by A. The point beyond which these fronts diverge is labeled D. As each species follows a rectangular isotherm, eventual constant pattern behavior is expected, resulting in uptake zones of constant width. One would not expect the presence of B to affect the uptake profile of A apart from possibly reducing its maximum adsorbed concentration, since A is the displacer.

Based on these observations, three major zones are expected: the zone where both A and B are simultaneously being adsorbed and B displaced (region I); the zone where species B is adsorbed to
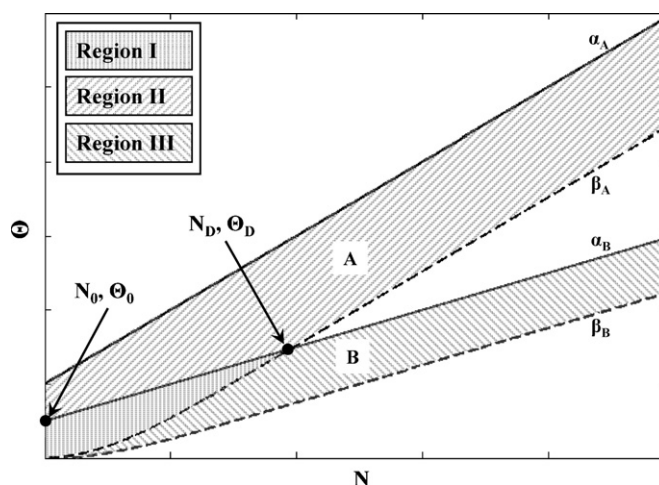

Fig. 2. Illustration of binary breakthrough behavior predicted by the shrinking core model, as a function of dimensionless column position, N, and dimensionless time, Θ. The upper and lower sets of lines correspond to the species A and B breakthrough zones, respectively. The solid lines, labeled α_i, represent the saturation boundaries ($R_i = 0$) and the dashed lines the depletion boundaries ($R_i = R_p$). The three cases for which uptake equations are derived correspond to the shaded regions of the graph. The labeled points represent key results from the species B solution, including the column inlet saturation time, point 0, and the binary divergence location, point D.

saturation but is being displaced by species A (region II); and the zone where species B is being taken up independently of species A (region III). Two of these labeled regions may be compared with constant-pattern zones illustrated in Cooney and Strusi [14], with region II corresponding to their zone II and region III corresponding to their zone IV.

In the single-component case the variables C_i and q_i represent the individual fluid and adsorbed concentrations, respectively. Superscript F represents the feed concentration, specifically for variables C_i^F and q_i^F, the feed concentration and the adsorbed concentration in equilibrium with the feed, respectively. In the binary case, equilibrium adsorbed concentrations are represented by q_{ij}^F, where i denotes the species of interest and j indicates the presence of the other binary component.

Dimensionless fluid concentration variables are defined as [4,7]:

$$X_i = \frac{C_i}{C_i^F} \quad \bar{X}_i = \frac{C_i^b}{C_i^F}$$

where the superscript b and the overbar on the mobile-phase concentration indicate bulk values, compared with local values within a particle. Adsorbed concentrations are defined differently for the two species, since A displaces B and is observed only with B present. Additionally, the dimensionless parameter Λ_i is defined similarly to a quantity used by Hall et al. [7]:

$$Y_A = \frac{q_A}{q_{AB}^F} \quad \bar{Y}_A = \frac{\bar{q}_A}{q_{AB}^F} \quad \Lambda_A = (1-\varepsilon)\frac{q_{AB}^F}{C_A^F}$$

$$Y_B = \frac{q_B}{q_B^F} \quad \bar{Y}_B = \frac{\bar{q}_B}{q_B^F} \quad \Lambda_B = (1-\varepsilon)\frac{q_B^F}{C_B^F}$$

The overbar on the adsorbed concentration indicates a particle volume-averaged value, rather than a local concentration as a function of radial position inside the particle. Based on these definitions, $\chi = (q_{BA}^F/q_B^F)$ is defined as the fraction of B remaining adsorbed after displacement by A; χ approaches a value of zero in the limit of complete displacement.

3.1. Balance expressions

If axial dispersion is neglected, the chromatographic balance equation [3] for each species may be written as a function of the dimensionless concentrations defined above as

$$\frac{\partial \bar{X}_i}{\partial t} + u \frac{\partial \bar{X}_i}{\partial z} = -\frac{\Lambda_i}{\varepsilon} \frac{\partial \bar{Y}_i}{\partial t} \tag{3}$$

Introducing the dimensionless time and axial position variables defined in Eqs. (1) and (2) results in the simplification of Eq. (3) to

$$\left(\frac{\partial \bar{X}_i}{\partial N} \right)_\Theta = -\frac{\Lambda_i}{\Lambda_A} \left(\frac{\partial \bar{Y}_i}{\partial \Theta} \right)_N \tag{4}$$

Intraparticle transport is assumed to be by pore diffusion, described by

$$\frac{\partial Y_i}{\partial t} = \frac{D_e^i (1-\varepsilon)}{\Lambda_i r^2} \frac{\partial}{\partial r} \left[r^2 \left(\frac{\partial X_i}{\partial r} \right) \right] \tag{5}$$

Because of the assumed rectangular isotherm, the adsorbed concentration in the region $R_A \le r \le R_p$ is constant, as shown in Fig. 1, yielding

$$\frac{dY_A}{dt} = \frac{dY_B}{dt} = 0 \tag{6}$$

in the respective ranges for the two species. Using this result as the left-hand side of Eq. (5) and integrating the right-hand side twice within the saturated zones for each respective species yields, with application of the boundary condition $X_i\big|_{r=R_i} = 0$ (see Fig. 1), the intraparticle concentration profiles

$$X_A(r) = X_A\big|_{r=R_p} \frac{[(1/R_A)-(1/r)]}{[(1/R_A)-(1/R_p)]} \quad R_A \le r \le R_p \tag{7a}$$

$$X_B(r) = \begin{cases} X_B\big|_{r=R_A} \dfrac{[(1/R_B)-(1/r)]}{[(1/R_B)-(1/R_A)]}, & R_A \le r \le R_p \\ X_B\big|_{r=R_A} + (X_B\big|_{r=R_p} - X_B\big|_{r=R_A}) \dfrac{[(1/R_A)-(1/r)]}{[(1/R_A)-(1/R_p)]}, & R_B \le r \le R_A \end{cases} \tag{7b}$$

Taking the mass balance around the intraparticle displacement front, R_A, from Martin et al. [36] and substituting dimensionless variables results in

$$\frac{1}{\beta} X_A\big|_{r=R_p} + X_B\big|_{r=R_p} = X_B\big|_{r=R_A} \frac{[1/R_B - 1/R_p]}{[1/R_B - 1/R_A]} \tag{8}$$

The parameter $\beta = \Lambda_A D_e^B / [\Lambda_B D_e^A (1-\chi)]$ is similar to an analog in Martin et al., the only difference being that the expression here normalizes mobile-phase concentrations with respect to column feed values rather than the infinite bath concentrations used in the batch case [36].

The external transport resistance is neglected in this derivation, and thus the particle surface concentrations are assumed to be equal to the bulk fluid concentrations, i.e. $X_i\big|_{r=R_p} = \bar{X}_i$. Additionally a dimensionless radial position is defined as $\eta_i = R_i/R_p$, following the convention of Cooper and Liberman [8], and differing from the notation used by Martin et al. [36].

Particle uptake expressions are developed below for the three different regions that result from the shrinking-core assumption (Fig. 2), depending on which of the two species are present. The first two of these cases were considered in the batch situation [36]: region I, with $0 < \eta_A < 1$ and $0 < \eta_B < 1$, and region II, with $0 < \eta_A < 1$ and $\eta_B = 0$. Region III, $\eta_A = 1$ and $0 < \eta_B < 1$, arises in the column model when the species B front completely overtakes the species A front and uptake occurs analogously to the single-component case [15].

3.2. Region I: simultaneous uptake of A and B

In this region, uptake of both A and B is considered. The uptake rates are calculated by taking the volume-average of Eq. (5) and substituting the concentration gradients at the particle surface obtained from Eq. (7) to yield

$$\frac{d\bar{Y}_A}{dt} = \frac{3D_e^A(1-\varepsilon)}{\Lambda_A R_p^2} \left(\frac{\bar{X}_A}{(1/\eta_A)-1} \right) \tag{9a}$$

$$\frac{d\bar{Y}_B}{dt} = \frac{3D_e^B(1-\varepsilon)}{\Lambda_B R_p^2} \left(\frac{\bar{X}_B - (1/\beta)(1/\eta_B - 1/\eta_A)(\bar{X}_A)/[(1/\eta_A)-1]}{(1/\eta_B)-1} \right) \tag{9b}$$

Scaling and substitution of the particle uptake expressions (Eq. (9)) into the chromatographic balances (Eq. (4)) provides relationships for the mobile phase concentrations as a function of N at constant Θ:

$$\frac{d\bar{X}_A}{dN} = \frac{1}{2} \frac{\bar{X}_A}{1-(1/\eta_A)} \tag{10a}$$

$$\frac{d\bar{X}_B}{dN} = \frac{1}{2}(1-\chi)\frac{\Lambda_B}{\Lambda_A} \left[\frac{\bar{X}_A + \beta\bar{X}_B}{1-(1/\eta_B)} - \frac{\bar{X}_A}{1-(1/\eta_A)} \right] \tag{10b}$$

Following the approach of Cooper and Liberman [8], the form of the solution is simplified by expressing the fractional particle uptakes in terms of the dimensionless uptake radii, η_i:

$$\bar{Y}_A = 1 - \eta_A^3 \tag{11a}$$

$$\bar{Y}_B = \chi + (1-\chi)(1-\bar{Y}_A) - \eta_B^3, \tag{11b}$$

from which Eq. (9) yields

$$6\eta_A^2 \frac{d\eta_A}{d\Theta} = \frac{\bar{X}_A}{1-(1/\eta_A)} \tag{12a}$$

$$6\eta_B^2 \frac{d\eta_B}{d\Theta} = \frac{(1-\chi)(\bar{X}_A + \beta\bar{X}_B)}{1-(1/\eta_B)} \tag{12b}$$

The boundary condition at the column entrance for breakthrough chromatography, $\bar{X}_A = \bar{X}_B = 1$, gives rise to a time-dependent solution at the column entrance ($N=0$) that is identical to the batch uptake solutions presented by Martin et al. [36]:

$$\Theta = 2\eta_A^3 - 3\eta_A^2 + 1 \tag{13a}$$

$$\Theta(1-\chi)(1+\beta) = 2\eta_B^3 - 3\eta_B^2 + 1 \tag{13b}$$

Axial concentration profiles may be obtained by simultaneously solving Eq. (10) and a transformed form of Eq. (12) written with N rather than Θ as the independent variable. Cooper and Liberman [8] showed for the single-component case that this could be done by introducing a dummy variable, generalized here for the binary system as $G_i(\eta_i)$, where

$$G_A(\eta_A) = 2\eta_A^3 - 3\eta_A^2 + 1 \tag{14a}$$

$$G_B(\eta_B) = \frac{2\eta_B^3 - 3\eta_B^2 + 1}{(1-\chi)(1+\beta)} \tag{14b}$$

This transformation is completed by defining the depletion boundary $N = \beta_A(\Theta)$, along which $\bar{X}_A = \bar{Y}_A = 0$ and thus $\eta_A = 1$ and $G_A = 0$, and introducing the analog $N = \beta_B(\Theta)$ corresponding to $\bar{X}_B = \bar{Y}_B = \bar{X}_A = 0$, so that $\eta_B = \eta_A = 1$ and $G_B = G_A = 0$ are assumed (Fig. 2). The transformation results in

$$\frac{\partial \eta_A}{\partial N} = \frac{1}{6} \frac{\eta_A^2 + \eta_A + 1}{\eta_A} \tag{15a}$$

$$\frac{\partial \eta_B}{\partial N} = \frac{1-\chi}{6} \frac{\eta_A^3(1-(D_e^B/D_e^A)) + \beta\Lambda_B/\Lambda_A \eta_B^3 - 1 - \chi\beta\Lambda_B/\Lambda_A}{\eta_B^2 - \eta_B} \tag{15b}$$

or in terms of the dummy variables

$$\frac{\partial G_A}{\partial N} = \eta_A^3 - 1 \tag{16a}$$

$$\frac{\partial G_B}{\partial N} = \frac{1}{1+\beta} \left[\eta_A^3 \left(1 - \frac{D_e^B}{D_e^A} \right) + \beta \frac{\Lambda_B}{\Lambda_A} \eta_B^3 - 1 - \chi\beta\frac{\Lambda_B}{\Lambda_A} \right] \tag{16b}$$

which are suitable for numerical integration.

Just as there exists a line bounding the depletion region, i.e., where $\bar{X}_i = \bar{Y}_i = 0$, there is a line bounding the saturation region, where $\bar{X}_i = \bar{Y}_i = 1$. For species A, this line is represented by $N = \alpha_A(\Theta)$ (Fig. 2), and $\bar{X}_A = \bar{Y}_A = 1$ means that $\eta_A = 0$ and $G_A = 1$. For species A, Cooper and Liberman's single-component result [8] is obtained, resulting in

$$N = \Theta - 1 \tag{17}$$

with the region beyond ($\Theta \geq 1$) representing the constant pattern region, in which the breakthrough profile of species A is fully developed and does not change as the front moves along the column.

A similar procedure is followed to obtain the saturation region boundary for species B. Along $N = \alpha_B(\Theta)$, the relations $\eta_B = 0$ and $G_B = 1$ are satisfied, resulting in

$$\frac{d\Theta}{dN} = \frac{1}{\bar{X}_A + \beta\bar{X}_B} \left[\left(\frac{D_e^B}{D_e^A} - 1 \right) \eta_A^3 + 1 + \chi\beta\frac{\Lambda_B}{\Lambda_A} \right] \tag{18}$$

Apart from differences in the definitions of dimensionless variables, the species A equations mirror Cooper and Liberman's single-component results [8] and allow analytical determination of species A profiles throughout the constant-pattern region. The solution derived for B may be obtained in region I by numerically integrating the coupled ordinary differential expressions, Eqs. (10) and (16), using Eq. (13) as a boundary condition at the column entrance ($N = 0$).

3.3. Region II: uptake of A into a particle saturated with B

In this region, uptake of A results in displacement of B, but because there is no residual capacity for B near the center of the particle, the equations for B must be modified. The previously derived uptake expressions for A remain the same. As before, the time derivative for uptake of B (Eq. (11)) is written as

$$3\eta_B^2 \frac{d\eta_B}{dt} = -(1-\chi)\frac{d\bar{Y}_A}{dt} - \frac{d\bar{Y}_B}{dt} \tag{19}$$

but the fractional uptake derivatives (Eq. (9)) are much simpler as a result of there being only displacement of B without any uptake. As a result the terms on the right-hand side cancel to give

$$6\eta_B^2 \frac{d\eta_B}{d\Theta} = -(1-\chi)\frac{\bar{X}_A}{(1/\eta_A)-1} + \frac{1}{\beta}\frac{D_e^B\Lambda_A}{D_e^A\Lambda_B}\frac{\bar{X}_A}{(1/\eta_A)-1} = 0 \tag{20}$$

confirming the invariance of η_B expected for particles already saturated with B. Transforming to the dummy variable $G_B(\Theta)$ yields

$$\frac{d\eta_B}{dN} = \frac{dG_B}{dN} = 0 \tag{21}$$

The derivative of the mobile-phase concentration in this region is non-zero as a result of displacement:

$$\frac{d\bar{X}_B}{dN} = -\frac{1}{2}(1-\chi)\frac{\Lambda_B}{\Lambda_A}\frac{\bar{X}_A}{1-(1/\eta_A)} \tag{22}$$

3.4. Region III: uptake of B

This case covers the eventuality of single-component uptake of species B after it overtakes A. Single-component linear driving force solutions for this profile have been derived previously [14,15]; the single-component shrinking-core mechanism is applied here.

The fractional uptake derivative in Equation 12b is modified, in this case due to the absence of A, resulting in

$$6\eta_B^2 \frac{d\eta_B}{d\Theta} = -\frac{D_e^B\Lambda_A}{D_e^A\Lambda_B}\frac{\bar{X}_B}{(1/\eta_B)-1} \tag{23}$$

Substitution into the chromatographic balance (Eq. (4)) results in

$$\frac{d\bar{X}_B}{dN} = \frac{1}{2}\frac{D_e^B}{D_e^A}\frac{\bar{X}_B}{1-(1/\eta_B)} \tag{24}$$

Following the same procedure as in the derivation of Eqs. (15) and (16), transformation of the derivative in Eq. (23) yields

$$\frac{\partial\eta_B}{\partial N} = \frac{1}{6}\frac{D_e^B}{D_e^A}\frac{\eta_B^2 + \eta_B + 1}{\eta_B} \tag{25}$$

or in terms of the dummy variable

$$\frac{\partial G_B}{\partial N} = \frac{\beta}{1+\beta}\frac{\Lambda_B}{\Lambda_A}(\eta_B^3 - 1) \tag{26}$$

Finally, expressing the saturation boundary in terms of $N = \alpha_B(\Theta)$ results in a boundary given by

$$\frac{d\Theta}{dN} = \frac{1}{\bar{X}_B}\frac{\Lambda_B}{\Lambda_A} \tag{27}$$

3.5. Analytical results

The derivation above was applied to each uptake regime in Fig. 2 and results in the complete specification of column behavior presented in Table 1. Based on these equations, column behavior may be predicted using numerical or analytical techniques. Analytical results have been obtained for simplified limiting cases of these equations, while numerical results may be obtained for all cases. The equations for G_A and η_A are restatements of the same equation, with η_A being preferable for analytical solution techniques and G_A for the numerical methods discussed later.

Table 1

Equations defining uptake behavior of each species in each of the three regions described in Fig. 2. Derivatives of all variables in the undefined regions of the plot are zero.

Derivative	Region I	Region II	Region III
$\frac{d\bar{X}_A}{dN} =$	$\frac{1}{2}\frac{\bar{X}_A}{1-(1/\eta_A)}$	$\frac{1}{2}\frac{\bar{X}_A}{1-(1/\eta_A)}$	0
$\frac{\partial\eta_A}{\partial N} =$	$\frac{1}{6}\frac{\eta_A^2+\eta_A+1}{\eta_A}$	$\frac{1}{6}\frac{\eta_A^2+\eta_A+1}{\eta_A}$	0
$\frac{\partial G_A}{\partial N} =$	$\eta_A^3 - 1$	$\eta_A^3 - 1$	0
$\frac{d\bar{X}_B}{dN} =$	$\frac{1}{2}(1-\chi)\frac{\Lambda_B}{\Lambda_A}\left[\frac{\bar{X}_A+\beta\bar{X}_B}{1-(1/\eta_B)} - \frac{\bar{X}_A}{1-(1/\eta_A)}\right]$	$-\frac{1}{2}(1-\chi)\frac{\Lambda_B}{\Lambda_A}\frac{\bar{X}_A}{1-(1/\eta_A)}$	$\frac{1}{2}\frac{D_e^B}{D_e^A}\frac{\bar{X}_B}{1-(1/\eta_B)}$
$\frac{\partial\eta_B}{\partial N} =$	$\frac{1-\chi}{6}\frac{\eta_A^3(1-(D_e^B/D_e^A))+\beta(\Lambda_B/\Lambda_A)\eta_B^3-1-\chi\beta(\Lambda_B/\Lambda_A)}{\eta_B^2-\eta_B}$	0	$\frac{1}{6}\frac{D_e^B}{D_e^A}\frac{\eta_B^2+\eta_B+1}{\eta_B}$
$\frac{\partial G_B}{\partial N} =$	$\frac{1}{1+\beta}\left[\eta_A^3\left(1-\frac{D_e^B}{D_e^A}\right) + \beta\frac{\Lambda_B}{\Lambda_A}\eta_B^3 - 1 - \chi\beta\frac{\Lambda_B}{\Lambda_A}\right]$	0	$-\frac{\beta}{1+\beta}\frac{\Lambda_B}{\Lambda_A}$

Analytical constant-pattern solutions for species A are considered first. As is apparent from the equations, the behavior of species A is completely independent of the presence of species B, so the integrated results for A always apply. As explained by Cooper and Liberman, the constant-pattern ($\Theta \geq 1$) solution for species A may be derived by integrating Eq. (15) using the $N = \alpha_A(\Theta)$ line in Eq. (17) as a limit of integration, resulting in

$$N - \Theta + 1 = \frac{\pi}{\sqrt{3}} + 3 \ln(\eta_A^2 + \eta_A + 1) - 2\sqrt{3}\tan^{-1}\left(\frac{2\eta_A + 1}{\sqrt{3}}\right) \quad (28)$$

a result differing only in the definitions of the independent variables from that of Cooper and Liberman [8]. This result is intuitively expected due to the stronger binding of species A and the absence of kinetic limitations on displacement. However, the presence of B is expected to decrease the maximum adsorbed concentration of A, an effect that is completely accounted for by basing this model on the adsorbed concentration of species A in the presence of B (q_{AB}^F). These analytical expressions govern the behavior of A through the remainder of this treatment. As would be expected, $\bar{X}_A = \bar{Y}_A$ in the constant-pattern region [8,12].

An analogous analytical result may be obtained for species B in region III beyond point D, which denotes the divergence of uptake zones for species A and B. Unlike species A, however, no universal analytical result exists for the $N = \alpha_B(\Theta)$ line, which is necessary for the completion of the integral defining the analytical solution. A limited result valid in region III may, however, be obtained. Since species A is absent in this region and the species B concentration is at its maximum due to displacement in region II, Eq. (18) simplifies to

$$\frac{d\Theta}{dN} = \frac{\Lambda_B}{\Lambda_A} \frac{1}{\bar{X}_B^{\max}} \quad (29)$$

Evaluation of Eq. (29) requires the maximum concentration of B in the mobile phase to be obtained. This result may easily be derived from the relationships above or from equilibrium displacement theory, where $\Delta\bar{q}_A/\Delta C_A^b = \Delta\bar{q}_B/\Delta C_B^b$ [2,13,18]. Both approaches are discussed further in Supplementary Material. In dimensionless form, the result is

$$\bar{X}_B = \frac{\Lambda_B}{\Lambda_A}(1 - \chi)(1 - \bar{X}_A) + 1 \quad (30)$$

or in the limit where species A is absent

$$\bar{X}_B^{\max} = \frac{\Lambda_B}{\Lambda_A}(1 - \chi) + 1 \quad (31)$$

Substitution of Eq. (31) into Eq. (29) allows evaluation of the $N = \alpha_B(\Theta)$ line in region III, given the existence of point D. Specification of this line then allows integration of Eq. (25), resulting in

$$\frac{D_e^B}{D_e^A}\left[N - \left(1 - \chi + \frac{\Lambda_A}{\Lambda_B}\right)(\Theta - \Theta_D) - N_D\right] = \frac{\pi}{\sqrt{3}} + 3\ln(\eta_B^2 + \eta_B + 1)$$

$$- 2\sqrt{3}\tan^{-1}\left(\frac{2\eta_B + 1}{\sqrt{3}}\right) \quad (32)$$

Using the definitions of the dimensionless variables N and Θ together with ideal chromatography theory to define the equilibrium column saturation trajectory gives

$$\frac{D_e^B}{D_e^A}\left[N_D - \left(1 - \chi + \frac{\Lambda_A}{\Lambda_B}\right)\Theta_D\right] = -1 \quad (33)$$

which allows Eq. (32) to be simplified to

$$\frac{D_e^B}{D_e^A}\left[N - \left(1 - \chi + \frac{\Lambda_A}{\Lambda_B}\right)\Theta\right] + 1 = \frac{\pi}{\sqrt{3}} + 3\ln(\eta_B^2 + \eta_B + 1)$$

$$- 2\sqrt{3}\tan^{-1}\left(\frac{2\eta_B + 1}{\sqrt{3}}\right) \quad (34)$$

This result allows η_B to be calculated throughout region III, with the stationary- and mobile-phase concentrations following from Eq. (11) and

$$\frac{\bar{X}_B}{\bar{X}_B^{\max}} = \bar{Y}_B \quad (35)$$

respectively. From these results, the concentration of B may be determined analytically throughout regions II and III, and additionally in the species B maximum overshoot zone between regions II and III.

The existence of the constant pattern solution for species B in region III (Eq. (34)) and its coincidence with equilibrium chromatography behavior appears not to be a general result, but it applies under certain isotherm conditions. A more thorough consideration of similar behavior in the linear driving force case is undertaken by Cooney and Strusi [14].

An additional analytical result of interest is obtained when the effective diffusivities of the two species are equal, in which case the $N = \alpha_B(\Theta)$ line (Eq. (29)) becomes valid over the entire column. Integrating Eq. (29) and evaluating the column entrance condition from Eq. (13) gives

$$\Theta = \frac{N + 1}{1 - \chi + (\Lambda_A/\Lambda_B)} \quad (36)$$

Apart from the equal-diffusivity case, the analytical solutions, taken together, span a significant fraction of the solution domain, obviating the need for numerical solutions. Analytical solutions are valid for all constant-pattern column regions, which are defined for species A as all $\Theta \geq 1$ and for species B as $\Theta \geq \Theta_D$. In practice, however, evaluation of the divergence point Θ_D can be a challenge, especially if it lies within the non-constant pattern region of species A ($0 < \Theta < 1$).

In the constant-pattern region of species A, the divergence point may be easily obtained from the results presented. Analytical expressions are known for the $\eta_B = 0$ (Eq. (34) with $\eta_B = 0$) and the $\eta_A = 1$ (Eq. (28) with $\eta_A = 1$) lines. Simple algebra allows the intersection point to be calculated as

$$\Theta_D = \frac{(D_e^A/D_e^B) - (\pi/\sqrt{3}) + 3\ln(3) - 1}{(\Lambda_A/\Lambda_B) - \chi}$$

$$N_D = \frac{(D_e^A/D_e^B) + ((-\pi/\sqrt{3}) + 3\ln(3) - 1)(1 + (\Lambda_A/\Lambda_B) - \chi)}{(\Lambda_A/\Lambda_B) - \chi} \quad (37)$$

which because of the constraint to the species A constant pattern region ($\Theta \geq 1$), applies for

$$\frac{\Lambda_A}{\Lambda_B} - \chi - \frac{D_e^A}{D_e^B} \leq -\frac{\pi}{\sqrt{3}} + 3\ln(3) - 1 \quad (38)$$

Fig. 3 illustrates this result graphically, where the constant-χ lines correspond to $\Theta_D = 1$, the limit of the constant pattern region for species A. Above each line, Eq. (37) gives Θ_D and the analytical solution for species B (Eq. (34)) is defined for all $\Theta \geq \Theta_D$. Below each line, Eq. (37) yields a physically meaningless result, and the analytical solution for species B is defined for the entire species A constant pattern region ($\Theta \geq 1$).

A final restriction is imposed on both the analytical and numerical solutions by the times required for the two species to saturate a single particle under batch uptake conditions. If the saturation time required for species B is greater than that for species A ($\Theta = 1$), displacement cannot occur because the species A front is adsorbing ahead of B. Using Eq. (13) to define this condition and simplifying yields an existence condition for the shrinking-core solution:

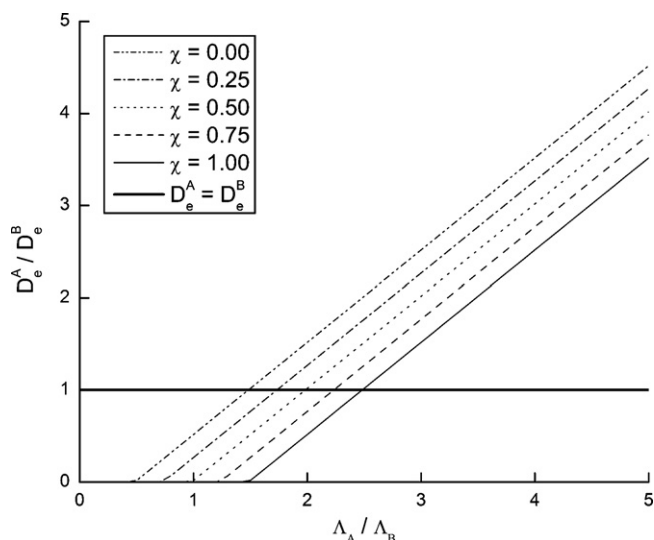$$\chi \leq \frac{\Lambda_A}{\Lambda_B}\frac{D_e^B}{D_e^A} \quad (39)$$

Fig. 3. Graphical representation of analytical solution restrictions defined in Eq. (38). Each line represents the parameter values for which $\Theta_D = 1$. Above each line the divergence point is defined analytically ($\Theta_D > 1$). Below each line the divergence point is undefined analytically ($\Theta_D < 1$). Shown for illustration is the equal diffusivity line, for which the species B trajectory is entirely defined analytically.

Fig. 4. Normalized mobile-phase concentration of B as a function of dimensionless time (Θ) and dimensionless axial column position (N). Solid lines indicate concentration profiles along the length of the column at fixed dimensionless times. The flat triangular region at the top of the plot indicates the region of maximum displacement ($\bar{X}_B^{max}$). Constant-pattern behavior is exhibited for all N and Θ values beyond the beginning of the maximum displacement region. Parameter values: $D_e^A = D_e^B$; $C_A^F = C_B^F$; $q_{AB}^F = q_B^F$; and $\chi = 0$.

For this condition switching the labels of species A and B would yield an appropriate description of behavior, as B would then be displacing A. This restriction is comparable to the ranking of binding strengths of various components in analysis of displacement in order to determine which species displace and are displaced [13,21,38].

3.6. Numerical solution

Numerical solutions were obtained using the ordinary differential equation suite in Matlab, specifically the function ode115. Equations were integrated with respect to N at a number of discrete Θ values using the time-dependent column inlet conditions, equal to the batch uptake results [36], as a boundary condition. Numerical continuity was assumed between different uptake regimes within the column. The simulation parameters were chosen to match real experimental or representative theoretical column conditions. Predicted chromatograms were obtained by plotting time points at a fixed simulated dimensionless axial position N.

Solutions were obtained by first calculating the time-dependent boundary conditions along the Θ-axis of Fig. 2. Lines $N = \alpha_i(\Theta)$, $\eta_i = 0$, were calculated based on the analytical solution profile for A (Eq. (28)), as these lines are necessary to determine the boundaries between solution regions. Appropriate coupled ODEs listed in Table 1 for mobile and stationary phase concentrations of each species were then integrated with respect to N, starting from the column entrance conditions given by Eq. (13). Integration was performed in terms of G_i rather than η_i because the G_i expressions are continuous until the end of the region of integration whereas the η_i expressions are discontinuous at the beginning of the region of integration.

Equations for integration were selected based on the solution regions illustrated in Fig. 2 and adjusted when different solution regions were encountered. The first adjustment is encountered when crossing one of the two $N = \alpha_i(\Theta)$, $\eta_i = 0$, lines defined above, and the second is when crossing the particle depletion boundaries, or $N = \beta_i(\Theta)$, $\eta_i = 1$. When such a trigger was reached, integration of the set of equations describing that region was terminated, and a new integration was begun using the set of equations describing the new region and the final values of the previous integration as
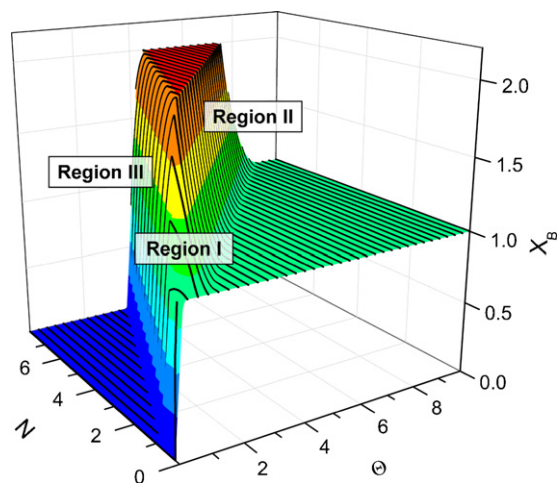
initial conditions. The latter adjustment for $N = \beta_i(\Theta)$, $\eta_i = 1$ is more difficult to calculate in advance, so region change was implemented when η_i approached to within some small tolerance of 1. Such approximations may introduce small errors into the numerical calculation, but the differences between the numerical and analytical results for species A even at a tolerance of 0.001 were negligible.

4. Results and discussion

4.1. General solution characteristics

Solutions have been obtained for a range of conditions to explore the effects of the model parameters on the predicted behavior. As expected, the predicted species A profiles always mirror the corresponding results for a single species [8], while the species B profiles exhibit a wider variety of behavior, but are always characterized by a solution development region and a constant-pattern, maximum-overshoot region. A sample profile for a reference set of parameter values is shown in Fig. 4.

Fig. 4 shows several clearly defined solution regions: region I is the entrance region at the forefront of the plot (small N); region II is the sloping region on the right side of the horizontal maximum; and region III is the sloping region on the left side of the horizontal maximum. Point D is the closest vertex of the triangle on top and indicates the beginning of the constant-pattern region. Beyond this point, all solutions may be obtained analytically. Additionally, the flat triangular portion is the maximum overshoot region, indicated by $\bar{X}_B^{max}$. The species A profile is not shown, but its breakthrough coincides with regions I and II described previously.

Cuts taken perpendicular to the Θ axis along the lines shown in Fig. 4 indicate the mobile-phase concentration as a function of dimensionless axial position at a fixed dimensionless time. Cuts taken perpendicular to the N axis indicate the mobile-phase concentration at a fixed axial position as a function of dimensionless time, i.e., results commonly seen in chromatograms. Fig. 5 shows the chromatograms for B for a number of cuts at various axial positions. The development of the constant-pattern region is clearly illustrated in these results.

The dimensionless model parameters that may be varied are the ratio of the pore diffusivities of the two species, the ratio of the Λ_i parameters containing the feed and bound concentrations, and the
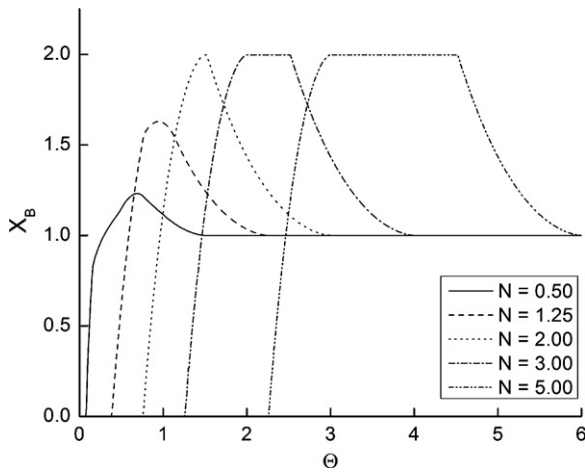
Fig. 5. Comparison of normalized mobile-phase concentrations of B as a function of dimensionless time at different fixed axial positions, under the same simulation conditions as in the surface plot in Fig. 4. Each successive cut shows the development of the constant-pattern, maximum-displacement region, which is reached at $N = 2$.

Fig. 7. Comparison of normalized mobile-phase concentrations of B for different diffusivity ratios as a function of dimensionless time. Parameter values: $N = 2$; $\Lambda_A = \Lambda_B$; and $\chi = 0$.

χ parameter indicating the fraction of displacement. Fig. 6 illustrates the effect of varying the Λ_A/Λ_B ratio. If all other parameters are held constant, this ratio increases with a decrease in the binding capacity or an increase in the feed concentration of species B. Increasing Λ_A/Λ_B ratios correspond to earlier breakthrough and smaller maximum overshoot values of B, a logical result since higher feed concentrations and lower binding capacities of B correlate with earlier breakthrough. Earlier breakthrough with respect to A then results in a wider displacement band and thus a lower maximum concentration of B.

The effect of varying the diffusivity ratio is shown in Fig. 7. A decrease in the ratio results in more diffuse uptake fronts of B, showing earlier initial breakthrough of B and later achievement of complete breakthrough, and vice versa. As illustrated clearly in Fig. 7, the diffusivity ratio does not have any impact on the maximum overshoot value achieved by B.

4.2. Comparison of model predictions with experiment

Experimental data for binary breakthrough chromatography of lysozyme and cytochrome c on SP Sepharose FF were obtained for
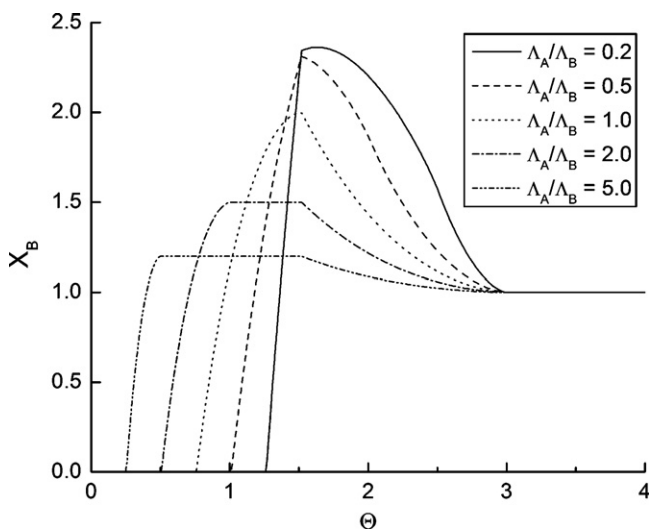

Fig. 6. Comparison of normalized mobile-phase concentrations of B at different $\Lambda_A/\Lambda_B = (q_{AB}^F/q_B^F)(C_B^F/C_A^F)$ ratios, as a function of dimensionless time. Parameter values: $N = 2$; $D_e^A = D_e^B$; and $\chi = 0$.
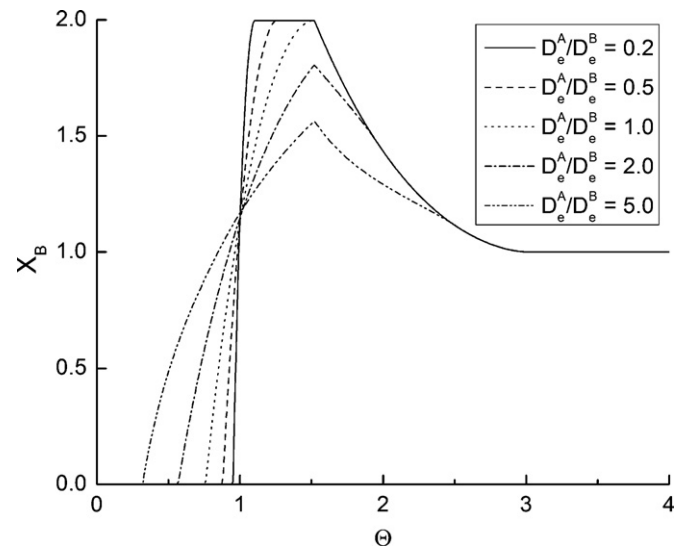
the flow rates, feed concentrations, and column parameters listed in Table 2; also shown are sources of the parameter values used in the simulations. Lysozyme represents species A, the displacer, and cytochrome c species B, the displaced species [36,37].

Results of binary shrinking core calculations performed in the non-constant pattern region using the parameter values in Table 2 are compared with experimental data in Fig. 8. Results obtained using two additional PDE models assuming a solid-film linear driving force model and a fitted colloidal isotherm [37] are also included for comparison; these equations were solved by finite differences [43]. In each case the rate of mass transfer was calculated based on a lumped mass transfer coefficient estimated using [44]

$$k_f^i = \frac{60 D_e^i C_i^F}{d_p^2 q_i^F} \tag{40}$$

In one case a global driving force was assumed, calculated from the feed and associated equilibrium concentrations, and in the other a local driving force was calculated at each mesh point based on local concentration and equilibrium values.

All the models capture the behavior of species A relatively well; since species A binds more strongly than and displaces B, this result

Table 2
Parameter values used in calculation of shrinking core solution in Figs. 8 and 9. Species A is lysozyme and species B is cytochrome c.

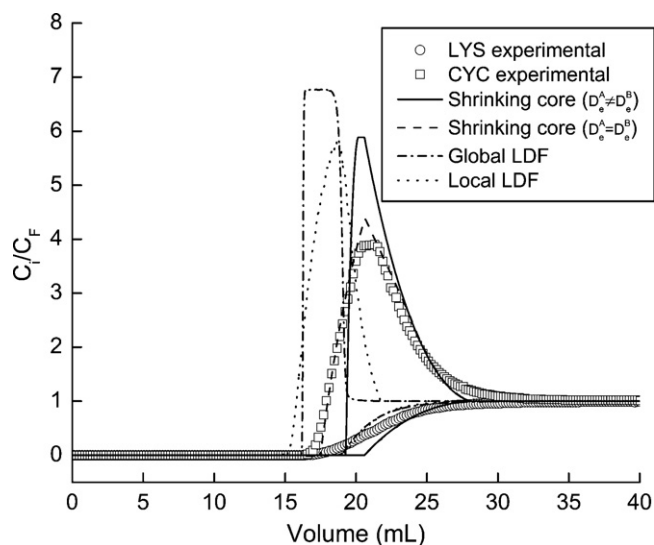|	Non-constant pattern (Fig. 8)	Constant pattern (Fig. 9)
C_A^F (mg/mL)	2.0	1.0
C_B^F (mg/mL)	0.2	0.7
q_B^F (mg/mL) [42]	100	100
q_{AB}^F (mg/mL) [37]	200	180
q_{BA}^F (mg/mL) [37]	2.0	2.0
D_e^A (cm^2/s) [31]	2.7×10^{-7}	2.7×10^{-7}
D_e^B (cm^2/s)	2.0×10^{-6} [36], 2.7×10^{-7}	2.0×10^{-6} [36], 2.7×10^{-7}
ε	0.35	0.37
u (interstitial, cm/h)	485	248, 413, 578
z (cm)	5.00	6.05
d_c (cm)	0.3	0.5
d_p (μm)	100	100

Fig. 8. Comparison of experimental (open symbols) and predicted shrinking core (solid lines) breakthrough curves for binary lysozyme/cytochrome c (LYS/CYC) breakthrough on SP Sepharose FF at pH 7 (experimental parameters in Table 2). A comparison is also shown for the case where the CYC diffusivity is taken as equal to the LYS diffusivity in the shrinking-core model (dashed line; overlaid by solid for LYS and part of CYC). Also shown are adaptations of the solid-film linear driving force (LDF) model, one using a global driving force based on the feed concentration and the other using a local driving force based on the local protein concentration.

Fig. 9. Comparison of experimental breakthrough curves (open symbols) and calculations using the analytical shrinking-core constant-pattern (solid lines) for the lysozyme/cytochrome c (LYS/CYC) system on SP Sepharose FF at pH 7 at linear interstitial velocities of 248 cm/h (a), 413 cm/h (b) and 578 cm/h (c) (experimental parameters in Table 2). A comparison is shown for the case where the CYC diffusivity is taken as equal to the LYS diffusivity in the shrinking-core model (dashed line; overlaid by solid for LYS and part of CYC). Also shown are solid-film linear driving force predictions (dotted lines).

is expected. However, poor agreement is observed between the solid-film linear driving force model and the experimental data for species B. In contrast, excellent agreement is observed between the experimental data and the two shrinking-core predicted results, without the use of any adjustable parameters. The comparison of model results suggests that uptake proceeds through a displacement mechanism rather than through competitive binding. The premature emergence of displaced B predicted by the LDF models is presumably a result of the lumped description of transport, which results in more rapid competitive displacement than for the shrinking-core model, which allows B displaced within a particle to migrate toward the center of the particle before being displaced later.

One area of uncertainty surrounds the correct value of the pore diffusivity for CYC, for which a measured value was not found in the literature. Since CYC and LYS are similar in size and have similar free-solution diffusivities [45], their true pore diffusivities in the same adsorbent should be similar. The higher value listed in Table 2 was reported by Martin et al. [36] from a regression of batch uptake data using the shrinking-core model, but the value – about 50% higher than that in free solution – suggests that the uptake may have included a contribution to transport by some other mechanism, e.g., surface diffusion [46]. The main difference between the predictions using the different diffusivity values is that higher overshoot values are predicted by use of the higher CYC diffusivity, resulting from faster particle saturation by CYC and hence the displacement of larger amounts of CYC as LYS uptake proceeds. The higher overshoot values are not observed experimentally (Fig. 8), possibly due to inapplicability of the reported diffusivity value in our experiments and/or additional contributions of dispersion and other limiting mass transfer effects.

A striking feature of the shrinking-core prediction is the sharpness of the edges relative to the experimental curves. For species A, the result is identical to that of Cooper and Liberman, with the sharp corner resulting from the shrinking-core assumption itself and the omission of external mass transfer resistance and axial dispersion effects. Inclusion of either or both of these effects would result in
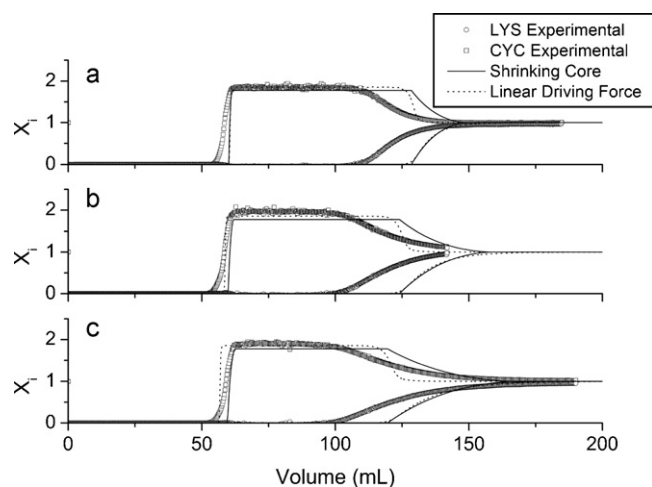
smoother curves and better qualitative agreement with the form of the experimental results [7,9].

In the case of species B, a sharp spike is observed, which correlates exactly with the position of the corner in the species A solution. Since species B is subject to displacement by species A, the effect of the corner in the A chromatogram is amplified here. Species B has a reasonably high affinity for the column, but cannot adsorb, and is in fact being displaced by species A. Once the displacement effect subsides, the remainder of the protein quickly adsorbs to the column. Again, it is expected that inclusion of the effects mentioned above would mitigate the discontinuous behavior and allow even better agreement with experimental data.

Analytical results of binary shrinking-core calculations performed in the constant-pattern region using the parameter values in Table 2 are compared with experimental data in Fig. 9. These results are also compared with predictions of a linear driving force model using the global driving force model described for Fig. 8.

Both the shrinking core and the linear driving force models capture the general trends exhibited in the experimental data. However, the calculated lysozyme results disagree somewhat with the experimental profiles, exhibiting later breakthrough than seen in practice. This late breakthrough results in additional discrepancies between experiment and simulation for cytochrome c. The difference in the breakthrough position for lysozyme reflects a discrepancy in the capacity, while the difference in slope can be affected also by transport effects. The discrepancies were seen also in single-component lysozyme breakthrough and were not resolved by direct measurement of column porosity, so their origin is unclear. However, the overall solution structure is correctly captured.

The difference in behavior observed in Fig. 8 between the two shrinking-core diffusivity parameters is limited to the non-constant pattern region, as diffusivity effects on maximum overshoot values are not observed in the constant pattern region, where the maximum overshoot is always reached. The higher reported apparent diffusivity [36] appears to predict CYC uptake rates better, as illustrated in Fig. 9.

Comparing predictions of the different models reveals that the LDF model again predicts early displacement of the cytochrome c, rather than the simultaneous displacement with lysozyme

binding predicted by the shrinking-core model and validated by experimental results. The effects of the LDF prediction of early displacement appear to be less significant in the constant-pattern regions (Fig. 9) than in the non-constant pattern regions (Fig. 8), as the larger volume of the constant-pattern displacement region tends to mask this error. Thus accounting for displacement effects through the shrinking-core model appears to have the most noticeable effect on solution accuracy for non-constant pattern regions. The superiority of the shrinking-core model in this regard is still observed in constant-pattern regions, but its effect on solution accuracy is less noticeable. Non-constant pattern regions tend to be observed for columns of physically relevant dimensions under conditions of moderate to higher flow rates and relatively low concentrations of the displaced species, conditions typical of those for an overloaded bind-and-elute separation step.

An additional comparison between models that is especially relevant in the constant-pattern case is simulation time. Constant-pattern regions tend to develop in a longer column over a longer period of time, requiring significant computational power to achieve a full numerical solution using discretization methods such as finite differences. Further, maximum front sharpness is achieved in this region, resulting in numerical convergence issues. The shrinking-core solution in this region has the advantage of being analytical, producing results of comparable or improved accuracy in a fraction of the computational time needed for a purely numerical solution.

5. Conclusions

The single-component shrinking core breakthrough model was solved for binary breakthrough chromatography for cases where one molecular species displaces another, allowing easier achievement of limited analytical and complete numerical solutions. Compared with other modeling methods, the analytical consideration of sharp concentration gradients within the particle provides significant advantages in both solution accuracy and efficiency. Analytical treatment of the column length required for constant-pattern behavior is especially useful, as this has been largely overlooked or approximated in previous models for binary breakthrough behavior. Numerical simulation of model results requires no solution of partial differential equations, and thus numerical results are obtained using Matlab's ode suite; this is a significant achievement compared with some other binary models accounting for diffusive intraparticle transport.

Numerical predictions for lysozyme–cytochrome c breakthrough on SP Sepharose FF based only on isotherm data, effective diffusivity measurements and characterization of column packing properties show excellent agreement with experimental breakthrough data in the non-constant pattern case. In particular, the simulation provides much better predictions than solid-film linear driving force models. Such a favorable comparison suggests that displacement rather than competitive binding is occurring. The shrinking-core model effectively predicts the location and size of displacement effects, correlating favorably with experimental data for both constant and non-constant pattern cases.

Primary limitations of the model include assumptions of near-rectangular isotherms and pore diffusion, and reasonable neglect of extra-particle transport resistance. Binding of many proteins on strong ion exchangers satisfies the particle uptake assumptions,

and extra-particle effects may be modulated by appropriate flow rate selection. Experimental verification of the shrinking-core uptake mechanism may be accomplished by confocal microscopy [31–35].

Acknowledgements

Appendix A. Supplementary data

Supplementary data associated with this article can be found, in the online version, at doi:10.1016/j.chroma.2011.02.020.

References

[1] G.S. Bohart, E.Q. Adams, J. Am. Chem. Soc. 42 (1920) 523.
[2] D. DeVault, J. Am. Chem. Soc. 65 (1943) 532.
[3] G. Guiochon, A. Felinger, D.G. Shirazi, A.M. Katti, Fundamentals of Preparative and Nonlinear Chromatography, Elsevier Academic Press, New York, 2006.
[4] T. Vermeulen, Ind. Eng. Chem. 45 (1953) 1664.
[5] E. Glueckauf, J.I. Coates, J. Am. Chem. Soc. (1947) 1315.
[6] A.S. Michaels, Ind. Eng. Chem. 44 (1952) 1922.
[7] K.R. Hall, L.C. Eagleton, A. Acrivos, T. Vermeulen, Ind. Eng. Chem. Fundam. 5 (1966) 212.
[8] R.S. Cooper, D.A. Liberman, Ind. Eng. Chem. Fundam. 9 (1970) 620.
[9] N.K. Hiester, T. Vermeulen, Chem. Eng. Prog. 48 (1952) 505.
[10] H.C. Thomas, J. Am. Chem. Soc. 66 (1944) 1664.
[11] E. Glueckauf, Proc. Roy. Soc. (Lond.) 186 (1946) 35.
[12] D.O. Cooney, E.N. Lightfoot, Ind. Eng. Chem. Fundam. 4 (1965) 233.
[13] D.O. Cooney, E.N. Lightfoot, Ind. Eng. Chem. Process Des. Dev. 5 (1966) 25.
[14] D.O. Cooney, F.P. Strusi, Ind. Eng. Chem. Fundam. 11 (1972) 123.
[15] W.J. Thomas, J.L. Lombardi, Trans. IChemE 49 (1971) 240.
[16] K. Miura, K. Hashimoto, J. Chem. Eng. Jpn. 12 (1979) 329.
[17] K. Miura, H. Kurahashi, Y. Inokuchi, K. Hashimoto, J. Chem. Eng. Jpn. 12 (1979) 281.
[18] H.K. Rhee, N.R. Amundson, Chem. Eng. Sci. 29 (1974) 2049.
[19] F.G. Helfferich, Ind. Eng. Chem. Fundam. 6 (1967) 362.
[20] F.G. Helfferich, Adv. Chem. (1968) 30.
[21] G. Klein, D. Tondeur, T. Vermeulen, Ind. Eng. Chem. Fundam. 6 (1967) 339.
[22] Z. Ma, G. Guiochon, J. Chromatogr. 609 (1992) 19.
[23] M.W. Balzli, A.I. Liapis, D.W.T. Rippin, Trans. IChemE 56 (1978) 145.
[24] J.W. Carter, H. Husain, Chem. Eng. Sci. 29 (1974) 267.
[25] N. Forrer, A. Butte, M. Morbidelli, J. Chromatogr. A 1214 (2008) 71.
[26] A.I. Liapis, D.W.T. Rippin, Chem. Eng. Sci. 33 (1978) 593.
[27] V. Natarajan, B.W. Bequette, S.M. Cramer, J. Chromatogr. A 876 (2000) 51.
[28] C.C. Huang, J.R. Fair, AIChE J. 34 (1988) 1861.
[29] E. Furuya, Y. Takeuchi, J. Chem. Eng. Jpn. 19 (1986) 62.
[30] Y. Takeuchi, T. Wasai, S. Suginaka, J. Chem. Eng. Jpn. 11 (1978) 458.
[31] G. Carta, A.R. Ubiera, T.M. Pabst, Chem. Eng. Technol. 28 (2005) 1252.
[32] S.R. Dziennik, E.B. Belcher, G.A. Barker, A.M. Lenhoff, Biotechnol. Bioeng. 91 (2005) 139.
[33] J. Hubbuch, T. Linden, E. Knieps, A. Ljunglof, J. Thommes, M.R. Kula, J. Chromatogr. A 1021 (2003) 93.
[34] A. Ljunglof, R. Hjorth, J. Chromatogr. A 743 (1996) 75.
[35] A. Ljunglof, J. Thommes, J. Chromatogr. A 813 (1998) 387.
[36] C. Martin, G. Iberer, A. Ubiera, G. Carta, J. Chromatogr. A 1079 (2005) 105.
[37] X.K. Xu, A.M. Lenhoff, J. Chromatogr. A 1216 (2009) 6177.
[38] D. Tondeur, G. Klein, Ind. Eng. Chem. Fundam. 6 (1967) 351.
[39] E. Arevalo, M. Rendueles, A. Fernandez, A. Rodrigues, M. Diaz, Sep. Purif. Technol. 13 (1998) 37.
[40] P.R. Jena, J.K. Basu, S. De, Chem. Eng. J. 102 (2004) 267.
[41] W.K. Teo, D.M. Ruthven, Ind. Eng. Chem. 25 (1986) 17.
[42] X.K. Xu, A.M. Lenhoff, J. Phys. Chem. B 112 (2008) 1028.
[43] M. Czok, G. Guiochon, Anal. Chem. 62 (1990) 189.
[44] M.D. LeVan, G. Carta, C. Yon, in: D.W. Green (Ed.), Perry's Chemical Engineers' Handbook, McGraw-Hill, New York, 1997.
[45] T.E. Creighton, Proteins: Structure and Molecular Properties, W.H. Freeman and Company, New York, NY, 1993.
[46] A.M. Lenhoff, Langmuir 24 (2008) 5991.